Applied Physics Letters ARTICLE pubs.aip.org/aip/apl

Quantification of magnetization of nanostructures via three complementary methods

Cite as: Appl. Phys. Lett. **126**, 242403 (2025); doi: 10.1063/5.0266886
Submitted: 21 February 2025 · Accepted: 1 June 2025 ·
Published Online: 16 June 2025

Xianhui Ye,[1] **Hangbo Su,**[1] **Jiaqi Su,**[1] **András Kovács,**[2] **Marco Beleggia,**[3] **Rafal E. Dunin-Borkowski,**[2] **and Zi-An Li**[1,a)]

AFFILIATIONS

[1] School of Physical Science and Technology, and State Key Laboratory of Featured Metal Materials and Life-Cycle Safety for Composite Structures, Guangxi University, Nanning 530004, China
[2] Ernst Ruska-Centre for Microscopy and Spectroscopy with Electrons (ER-C 1) and Peter Grünberg Institute (PGI 5), Forschungszentrum Jülich GmbH, 52425 Jülich, Germany
[3] Department of Physics, University of Modena and Reggio Emilia, 41125 Modena, Italy

[a)] **Author to whom correspondence should be addressed:** zianli@gxu.edu.cn

ABSTRACT

The quantitative measurement of magnetization in magnetic nanostructures plays a crucial role in advancing both fundamental understanding and applied research. Off-axis electron holography in a transmission electron microscope enables the retrieval of magnetic phase shifts induced by magnetic induction fields, thereby allowing precise quantification of magnetization. Using magnetite (Fe_3O_4) nanoparticles as a model system, we use off-axis electron holography to demonstrate three complementary methods for quantifying the magnetic properties of nanoparticles. These methods are the simple geometric approximation, the magnetic phase gradient integration, and the model-based iterative reconstruction, each providing unique capability, ranging from the rapid estimation of in-plane magnetic induction to highly detailed spatially resolved magnetization maps. We analyze the strengths, the limitations, and the applicability of each approach, emphasizing the potential of integrating these methods for a comprehensive analysis of the magnetization of nanomaterials.

The precise measurement of magnetic moments at the nanoscale is fundamental to materials science and nanotechnology. At this scale, magnetic properties differ significantly from those of bulk materials, giving rise to phenomena such as superparamagnetism,[1] enhanced magnetic anisotropy, and quantum mechanical effects,[2,3] which are critical for advancing data storage, spintronics, and biomedical applications. Accurate quantification of magnetic moments is essential for understanding nanoscale magnetic systems and optimizing their performance.[4–6]

However, nanoscale measurements present significant challenges. Weak, localized magnetic fields require sensitive methods with nanometer-scale spatial resolution.[7,8] Conventional techniques, such as superconducting quantum interference device magnetometry and vibrating sample magnetometry, lack the necessary spatial resolution. Although scanning probe methods like magnetic force microscopy and Kerr microscopy offer improved resolution, they primarily detect stray field gradients or surface signals and do not directly probe the internal magnetization distribution.

Transmission electron microscopy (TEM)-based techniques provide more direct access to magnetic information with high spatial resolution. Differential phase contrast (DPC) imaging and electron magnetic circular dichroism (EMCD) are effective for probing magnetic properties.[9,10] DPC directly maps magnetic induction with high spatial resolution, while EMCD provides insights into spin and orbital moments through electron energy-loss spectroscopy. In addition, a range of computational phase retrieval techniques has been developed for magnetic imaging using Lorentz TEM and four-dimensional scanning transmission electron microscopy. These methods provide improved phase sensitivity and spatial resolution and have been employed to reconstruct complex magnetic textures, including noncollinear spin configurations and topological defects in skyrmion systems.[11–15]

Among various TEM-based techniques, off-axis electron holography (EH) is well established as a powerful method for analyzing electromagnetic fields in nanoscale materials.[16–18] By using an electrostatic biprism to interfere an electron wave passing through the sample with a reference wave, EH encodes phase shifts related to both electrostatic potentials and magnetic vector potentials. This enables simultaneous high-resolution mapping of electrostatic and magnetic fields,[19] making EH ideal for studying magnetic nanostructures.

In this work, we apply off-axis electron holography to quantitatively analyze the magnetic properties of Fe_3O_4 nanoparticles using three complementary methods: the geometric approximation, magnetic phase integration, and model-based iterative reconstruction (MBIR).[20–22] The geometric approximation provides a rapid estimate of projected in-plane magnetic induction, suitable for initial assessment. The magnetic phase integration enables model-independent measurements of total magnetic moments, particularly for irregularly shaped particles or complex domain structures. The MBIR method achieves high spatial resolution, offering detailed magnetization maps of individual nanoparticles. By combining these methods, we are able to rapidly assess the magnetic moment distribution at the nanoscale and perform detailed analysis.

Off-axis electron holography in a transmission electron microscope is commonly used for quantitative analysis of electric and magnetic fields in nanostructures. Figure 1(a) shows a schematic of the experimental setup, where part of the electron wave interacts with the sample, and the other part passes through the vacuum as a reference wave. The resulting interference pattern encodes phase differences proportional to the projected electrostatic potential $V(\boldsymbol{r})$ and magnetic vector potential $\boldsymbol{A}(\boldsymbol{r})$ as shown by[23]

$$\varphi(\mathbf{r}) = C_E \int_{-\infty}^{+\infty} V(\mathbf{r})\,\mathrm{d}z - \frac{\pi}{\phi_0}\int_{-\infty}^{+\infty} A_z(\mathbf{r})\cdot \mathrm{d}z, \qquad (1)$$

where $\varphi(\boldsymbol{r})$ is the phase shift, C_E is an interaction constant that depends on the accelerating voltage of the electron microscope ($C_E = 6.53\mathrm{radV}^{-1}\,\mu\mathrm{m}^{-1}$ for 300 kV electrons), ϕ_0 is the flux quantum $h/2e = 2.07\times 10^3\mathrm{Tnm}^2$. The electrostatic potential $V(\boldsymbol{r})$ includes the mean inner potential (MIP) of the sample and electrostatic stray fields,[24] while $A_z(\boldsymbol{r})$ is the z-component of the magnetic vector potential. The first term represents the electrostatic contribution, and the second term corresponds to the magnetic contribution.

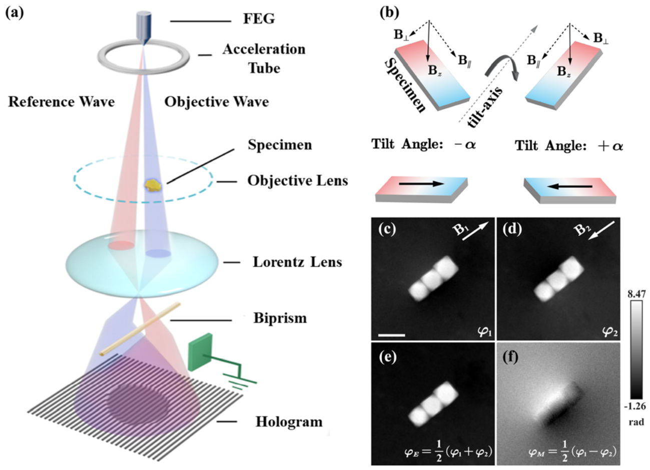

FIG. 1. (a) Schematic diagram illustrates the off-axis electron holography setup. (b) The *in situ* magnetization process, which involves tilting the specimen and applying magnetic fields to the specimen by activating objective lens. (c) and (d) A pair of reconstructed total phase images of the specimen, with reversed magnetization states. (e) and (f) Corresponding electrostatic and magnetic phase images, respectively, obtained by calculating half of the sum and half of the difference between the phase images in (c) and (d). The scale bar represents 100 nm.

This phase information allows detailed mapping of the electrostatic and magnetic fields within and around nanostructures.

Off-axis electron holograms were acquired in Lorentz mode using an aberration-corrected FEI Titan 80–300 transmission electron microscope equipped with a holography setup at Forschungszentrum Jülich. The microscope features an ultra-high brightness field emission gun and a wide-gap pole piece. A gold-coated electrostatic biprism ($<$600 nm diameter) located at the selected area aperture was biased at 130 V to generate interference between object and reference waves, producing fringes with 2.7 nm spacing. Using one-third of the sideband, the spatial resolution was approximately 8 nm. Magnetic field distributions were derived from phase shifts via *in situ* magnetization. To correct phase artifacts from lens aberrations and biprism charging, reference holograms were recorded under identical conditions. Phase images were reconstructed using Fourier transformation and bandpass filtering with custom-coded Python scripts.

To accurately separate the magnetic contribution from the MIP in the phase shift, we employ an *in situ* magnetization reversal approach as shown in Fig. 1(b).[25] The sample was tilted to ±60°, and a magnetic field of approximately 1.5 T was applied via the microscope objective to reverse the magnetization of the nanoparticles along the electron beam. After the reversal, the objective lens was deactivated, the sample tilt restored to 0°, and the Lorentz lens used for holographic imaging under zero external magnetic field, preserving the remanent magnetization. Phase images were recorded for both magnetization states, enabling a robust separation of the electrostatic and magnetic contributions. The difference in phase images under the two magnetization states reveals that the magnetic potential is opposite in each state. Figures 1(c) and 1(d) show the phase maps after applying opposite magnetic fields. The contributions of the magnetic and electrostatic potentials are then calculated, and the MIP is subtracted from the phase images.

To investigate the static magnetic structure of magnetic nanoparticles in the remanent state, we used electron holography (EH) to study chain-like assemblies of magnetite (Fe_3O_4) nanoparticles and their associated magnetic induction. Figure 2(a) shows the magnetic contribution to the phase shift. The phase contours reveal the stray field emanating from the nanoparticle chain, showing that each particle contains a single magnetic domain [Fig. 2(b)]. No specific phase contrast related to domain walls was observed, indicating that the chain exhibits a uniformly magnetized state, with the magnetization direction aligned along the axial direction of the chain.

Figure 2(c) shows a line profile of the magnetic phase contribution, taken along the red dashed line passing through the center of the middle nanoparticle. The projected in-plane magnetic induction of each particle was determined by fitting a simulation to the experimental profile, using approximations of the nanoparticles as cubic and spherical geometries (details provided in the supplementary material).[26,27] For a uniformly magnetized sphere with radius a, the projected magnetic induction $B_\perp$ leads to the following phase shift expression:[20]

$$\varphi(x,y)|_{(x^2+y^2)>a^2} = \frac{e}{\hbar} B_\perp a^3 \left(\frac{x}{x^2+y^2}\right), \qquad (2)$$

where e is the elementary charge and $\hbar$ is the reduced Planck's constant, $B_\perp = (2/3)\mu_0 M_0$ for a spherical magnetic particle, and M_0 is the magnetization of the material. For a line profile taken through the

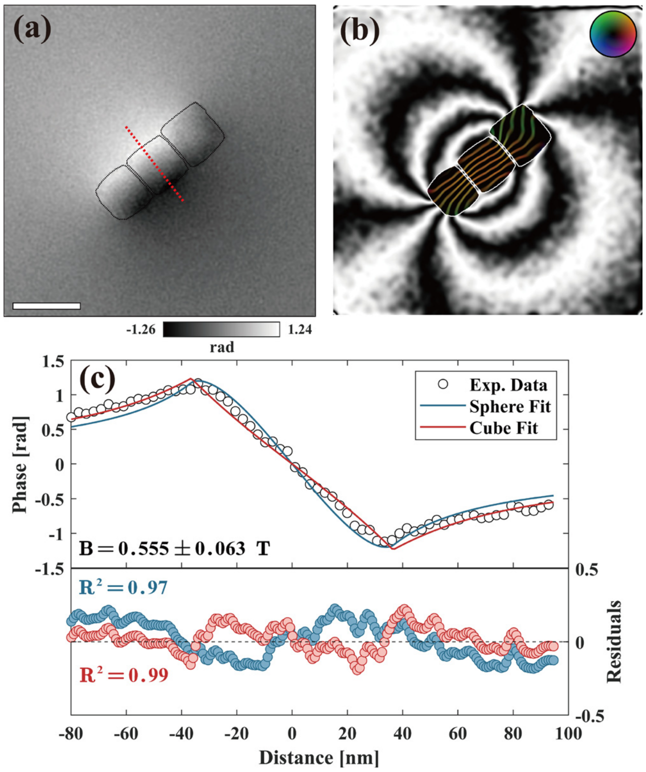

FIG. 2. (a) Experimental magnetic phase image of the Fe_3O_4 particles, black dashed lines outlining the particle contours, with a red dashed line indicating the axis positions for phase profile extraction. The scale bar represents 100 nm. (b) Color-coded equal-phase map, constructed from the cosine of the original magnetic phase image magnified 20 times, illustrating the projected in-plane magnetic induction field distributions within and around the Fe_3O_4 particles. The direction of the measured magnetic induction corresponds to the color wheel shown in (b). (c) The white scatter points represent the extracted phase profiles along the lines marked in (a). The two curves correspond to the least squares fits of the phase profiles generated using spherical and cubic geometries, respectively. The lower part of the figure presents the residual analysis for both fitted curves. The cubic fit reveals a saturation magnetic induction of 0.555 ± 0.063 T.

center of the particle in a direction perpendicular to $B_\perp$, the expression simplifies to

$$\varphi(x)|_{x>a} = \frac{e}{\hbar} B_\perp \left(\frac{a^3}{x}\right). \tag{3}$$

By fitting the experimental data to these equations, the best-fit value for the projected magnetic induction was found to be $B_\perp = 0.580 \pm 0.064$ T for the spherical fit and $B_\perp = 0.555 \pm 0.063$ T for the cubic fit, as shown in Fig. 2(c). Although the spherical fit is close to the saturation magnetic induction of magnetite, the cubic fit provides a better fit, and thus the final result is based on the cubic fit.

As previously mentioned, the method of approximation using simple geometric shapes is straightforward and intuitive, making it suitable for preliminary analysis of single particles with regular shapes. However, it is limited by the geometric approximation and the assumption of uniform magnetization, leading to model-dependent results with a constrained range of applicability. To obtain more quantitative information about the magnetic properties, we also applied a model-independent method based on magnetic phase integration to determine the magnetic moment of the particle from the phase images. This method integrates the magnetic phase, allowing for the direct measurement of the magnetic moment of isolated magnetic nanoparticles. As a result, it is less sensitive to factors such as particle shape and magnetic domain structure.

The magnetic moment can be obtained from the relation $\boldsymbol{m} = \iiint \boldsymbol{M}(r)\mathrm{d}^3\boldsymbol{r}$, where $\boldsymbol{M}(r)$ is the position-dependent magnetization, and $\boldsymbol{r}$ is the three-dimensional position vector. The electron holography phase images do not directly provide information about $\boldsymbol{M}(r)$, instead, they are proportional to the projection of the in-plane components of the magnetic induction $\boldsymbol{B}(r)$ within and around the particle along the electron trajectory. If the phase gradient is integrated over a portion of the field of view, a proportionality can be established between the integrated phase and the volume integral of the magnetic induction,[21]

$$\frac{\hbar}{e}\left[\hat{\boldsymbol{z}} \times \iint \nabla\varphi(\boldsymbol{r}_\perp)\mathrm{d}^2\boldsymbol{r}_\perp\right] = \iiint \boldsymbol{B}(\boldsymbol{r})\mathrm{d}^3\boldsymbol{r}. \tag{4}$$

This quantity $\boldsymbol{m}_\mathrm{B} = (1/\mu_0)\iiint \boldsymbol{B}(\boldsymbol{r})\mathrm{d}^3\boldsymbol{r}$ is referred to as the "inductive moment." The relationship between the magnetic moment $\boldsymbol{m}$ and the inductive moment $\boldsymbol{m}_\mathrm{B}$ can be established when the region of integration is a circle that encompasses all magnetized elements. In this case, the relationship is given by $\boldsymbol{m}_\mathrm{B} = (1/2)\boldsymbol{m}$. The magnetic moment of an isolated particle can be quantitatively determined by integrating the magnetic phase shift along a circular contour surrounding the particle. The integration path consists of concentric circles with radii gradually decreasing from R_2 to R_1, where the innermost circle lies close to the boundary of the magnetite nanoparticle chain, as shown in Fig. 3(a). The magnetic moment is obtained by extrapolating the integral results to zero integration radius, as illustrated in Fig. 3(b), in order to reduce systematic errors arising from fringe field contributions and phase noise. In this process, the loop integral is decomposed into two orthogonal components corresponding to the x- and y-directions, whose values are separately plotted in Fig. 3(b). This loop integral yields a vector magnetic moment, which can be decomposed into two orthogonal components corresponding to the x- and y-directions (details provided in the supplementary material).

The measured projected in-plane magnetic moment is $2.54 \times 10^7\ \mu_B$, with the direction indicated by the black arrow in Fig. 3(a). By estimating the volume of the magnetic particles from dimensions measured in the bright-field TEM image, the average magnetization was deduced to be $(2.206 \pm 0.014) \times 10^5$ A/m, corresponding to (0.280 ± 0.002) T, which is lower than the expected value of 0.6 T for magnetite. We will discuss the causes leading to this discrepancy in the next method.

Since the obtained results represent only half of the expected saturation magnetization, several factors were considered. Electron holography (EH) records magnetic information projected along the electron beam trajectory, measuring only the in-plane components of the magnetic moment while neglecting any out-of-plane contributions.[28] Furthermore, the misalignment between the magnetocrystalline easy axis ([1 1 1] direction) and the long axis of the nanoparticle chain ([1 0 0] direction) introduces a competition between magnetocrystalline anisotropy and shape anisotropy. Upon removal of the external magnetic field, magnetocrystalline anisotropy tends to align the

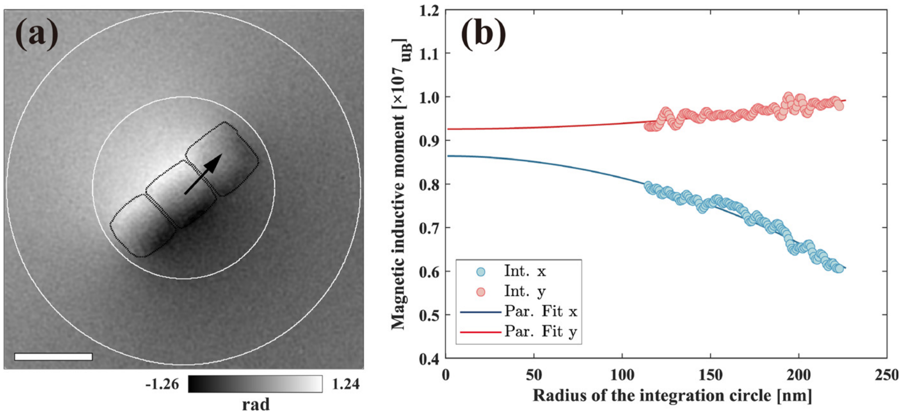

FIG. 3. (a) Measurement of the projected magnetic moment in the experimental magnetic phase image of Fe_3O_4 particles using circular loop integrals. The white circles indicate the minimum and maximum measurement radii. The scale bar represents 100 nm. (b) Results of the loop integral measurements from (a).

magnetic moments to the magnetic easy axis, while shape anisotropy favors alignment along the chain axis. This effect is more pronounced at the ends of the chain, where the weaker dipole–dipole interactions reduce the constraint on magnetic moments. As a result, the magnetic moments at the chain ends are more susceptible to boundary effects, leading to deviations in magnetization direction and the emergence of curvature or rotational effects. To address these issues, we explore the MBIR method to measure the projected in-plane magnetization distribution within the chain. This method links the magnetic vector potential $\boldsymbol{A}(r)$ from Eq. (1) to the magnetization distribution $\boldsymbol{M}(r)$ through convolution integration,[29]

$$\boldsymbol{A}(\boldsymbol{r}) = \frac{\mu_0}{4\pi}\int \boldsymbol{M}(\boldsymbol{r}') \times \frac{\boldsymbol{r}-\boldsymbol{r}'}{|\boldsymbol{r}-\boldsymbol{r}'|^3}\,\mathrm{d}\boldsymbol{r}', \tag{5}$$

allowing for the reconstruction of the magnetization distribution, particularly suited for complex or multi-particle systems.

Simulated magnetic phase images were generated by iteratively refining guesses of the in-plane magnetization distribution. We used analytical phase shift solutions for simple geometries and numerical discretization to avoid Fourier-space artifacts. Forward simulations solved the inverse problem of reconstructing the magnetization distribution. In-plane magnetization values were then derived based on the measured sample thickness. Detailed description of the MBIR method can be found in the dissertation.[22]

Since electron holography provides 2D projected magnetic information along the electron trajectory, the reconstructed magnetization corresponds to a slice with a thickness of one pixel (with a sampling rate of $a = 0.9029\,\mathrm{nm/pixel}$). Based on the MIP value of the sample (details provided in the supplementary material), the thickness was estimated at $t = 73\,\mathrm{nm}$, requiring a correction factor of a/t to obtain the true volume density of the magnetic moment. The reconstructed in-plane magnetization distribution is shown in Fig. 4(a), and its magnitude in Fig. 4(b). Due to potential out-of-plane magnetization at the particle ends, the uniform in-plane magnetization of the middle particle was selected for histogram analysis [Fig. 4(c)].

A Gaussian fit to the magnetic induction histogram yields a central value of 0.606 T with a width of 0.031 T, corresponding to a standard deviation of approximately 0.022 T. This result indicates that the magnetic moments remain aligned across the region, with minimal spatial variation, suggesting a well-defined uniform magnetization. Considering both thickness uncertainty and measurement errors (details provided in

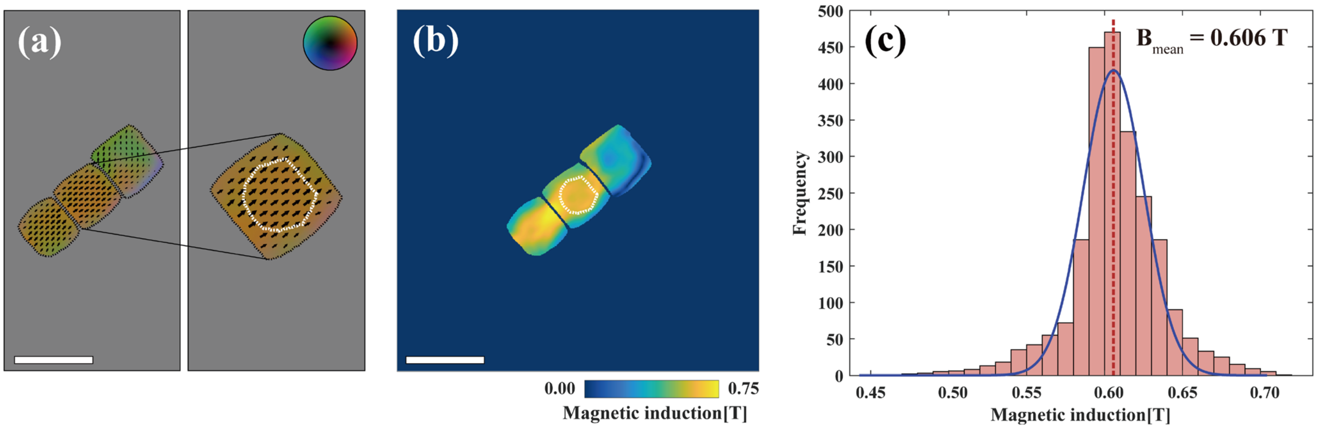

FIG. 4. (a) Projected in-plane magnetization distribution that was reconstructed from the experimentally acquired phase image. On the right is the projected in-plane magnetization distribution of the middle particle. (b) The magnitude map of the reconstructed magnetization distribution of the selected region. The selected region is indicated by a white dashed line. The scale bar represents 100 nm. (c) Histogram of selected region with the Gaussian fit mean indicated by the red dashed line at 0.606 T.

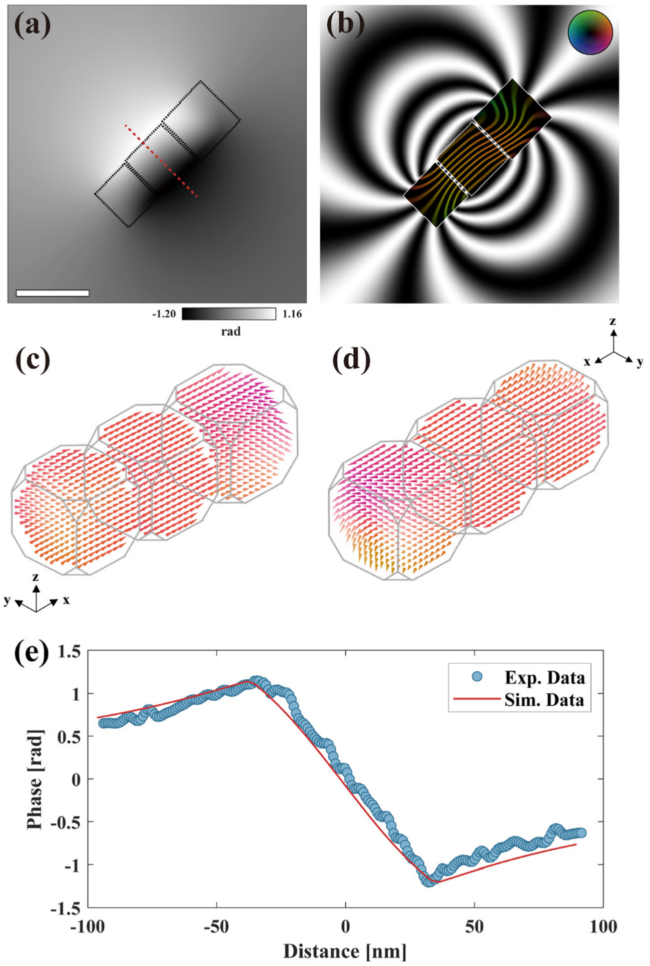

FIG. 5. (a) Simulated magnetic phase shift image with black dashed lines marking particle contours and a red dashed line indicating the phase profile axis. The scale bar represents 100 nm. (b) Color-coded equal-phase map from the cosine of the magnetic phase image, showing the in-plane magnetic induction of the Fe_3O_4 particles. The induction direction follows the inset color wheel. (c) and (d) The magnetization obtained by the simulated truncated cube in the equilibrium state, shown from two different viewing angles. (d) Comparison of experimental and simulated profiles along the red dashed line indicated in (a).

the supplementary material), the total average magnetization is 0.606 ± 0.031 T, in close agreement with the literature value of 0.6 T for magnetite. Summing the magnetic moments of all relevant voxels, the total magnetic moment is $2.37 \times 10^{-15}\ \mathrm{Am}^2 = 2.56 \times 10^7\ \mu_B$, nearly identical to the value of $2.35 \times 10^{-15}\ \mathrm{Am}^2 = 2.54 \times 10^7\ \mu_B$ from the magnetic phase integration method.

To facilitate comparison with experimental results, we carried out micromagnetic simulations using MuMax3[30] to determine the equilibrium magnetic configuration of the nanoparticles. Bulk values of Fe_3O_4 were adopted for the exchange stiffness, saturation magnetization, and magnetocrystalline anisotropy[31,32] (details provided in the supplementary material). From the simulated magnetization distribution, the corresponding magnetic phase shift image was subsequently calculated. The results show that the first two nanoparticles in the chain exhibit axially aligned single-domain states, whereas the third nanoparticle adopts a characteristic vortex configuration, as illustrated in Figs. 5(c) and 5(d). Similar transitions in magnetic states, governed by the interplay of particle size, shape, and magnetocrystalline anisotropy, have also been reported in Fe nanocubes, where a progression from uniform single-domain structures to vortex-like or more complex spin textures was systematically observed.[33,34] A close correspondence between our simulated and experimental phase shift maps is confirmed by the quantitative agreement of the extracted phase profiles, as shown in Fig. 5(e).

Here, we systematically evaluated three methods for analyzing the magnetic properties of magnetite nanoparticles using off-axis electron holography: the geometric approximation, magnetic phase integration, and the MBIR method. Each approach offers distinct advantages depending on specific analysis requirements. The geometric approximation provides a fast and efficient estimate of in-plane magnetic induction but is limited by assumptions of uniform magnetization and spherical geometry, making it less suitable for complex systems. The magnetic phase integration method, while model-independent and adaptable to irregular or multi-domain particles, yields only an average magnetic moment and cannot resolve spatial variations, particularly in larger particles supporting vortex states where stray fields vanish. In contrast, the MBIR method enables detailed mapping of projected in-plane magnetization distributions. Although its spatial resolution is constrained by mask application and regularization, this limitation can be mitigated using phase shift holography, improving the resolution to the intrinsic limit of recorded holograms.[35,36] Furthermore, by combining experimental observations with micromagnetic simulations, we verified the applicability of these methods, providing useful guidance for future studies on the magnetization behavior of complex nanoparticle systems.

See the supplementary material for details on the experimental conditions, data processing, and micromagnetic simulations.

The authors thank the Natural Science Foundation of Guangxi Province (No. 2024GXNSFDA010014), the Guangxi Science and Technology Major Program (No. AA23073019), the National Natural Science Foundation of China (No. 12364018), and the Innovation Project of Guangxi Graduate Education (Nos. YCBZ2022049 and YCBZ2023015) for their financial support. AK and RDB acknowledge funding from the European Research Council under the European Union's Horizon 2020 Research and Innovation Programme (Grant No. 856538, project "3D MAGiC"). The Center for Instrumental Analysis of Guangxi University is also acknowledged for providing research facilities and resources for the experiments.

AUTHOR DECLARATIONS

Conflict of Interest

The authors have no conflicts to disclose.

Author Contributions

Xianhui Ye: Data curation (lead); Formal analysis (lead); Visualization (lead); Writing – original draft (lead). **Hangbo Su:** Validation (supporting); Writing – review & editing (supporting). **Jiaqi Su:** Validation (supporting); Writing – review & editing (supporting). **András Kovács:** Validation (supporting); Writing – review & editing (supporting). **Marco Beleggia:** Validation (supporting); Writing – review & editing (supporting). **Rafal E. Dunin-Borkowski:** Validation (supporting); Writing – review & editing (supporting). **Zi-An Li:** Conceptualization (equal); Funding acquisition (lead); Methodology (equal); Project administration (lead); Resources (lead); Writing – review & editing (supporting).

DATA AVAILABILITY

The data that support the findings of this study are available from the corresponding author upon reasonable request.

REFERENCES

[1] M. Hu, H.-J. Butt, K. Landfester, M. B. Bannwarth, S. Wooh, and H. Thérien-Aubin, ACS Nano **13**, 3015 (2019).
[2] D. Song, Z.-A. Li, J. Caron, A. Kovács, H. Tian, C. Jin, H. Du, M. Tian, J. Li, J. Zhu *et al.*, Phys. Rev. Lett. **120**, 167204 (2018).
[3] C. Jin, Z.-A. Li, A. Kovács, J. Caron, F. Zheng, F. N. Rybakov, N. S. Kiselev, H. Du, S. Blügel, M. Tian *et al.*, Nat. Commun. **8**, 15569 (2017).
[4] R.-Y. Huang, Z.-H. Liu, W.-H. Weng, and C.-W. Chang, J. Mater. Chem. B **9**, 4267 (2021).
[5] D. Rist, T. DePalma, E. Stagner, M. M. Tallman, M. Venere, A. Skardal, and Z. D. Schultz, ACS Sens. **8**, 4636 (2023).
[6] J. M. Paez-Muñoz, F. Gámez, Y. Fernández-Afonso, R. Gallardo, M. P. Leal, L. Gutiérrez, J. M. de la Fuente, C. Caro, and M. L. García-Martín, J. Mater. Chem. B **11**, 11110 (2023).
[7] L. Rondin, J.-P. Tetienne, S. Rohart, A. Thiaville, T. Hingant, P. Spinicelli, J.-F. Roch, and V. Jacques, Nat. Commun. **4**, 2279 (2013).
[8] Y. Dovzhenko, F. Casola, S. Schlotter, T. X. Zhou, F. Büttner, R. L. Walsworth, G. S. Beach, and A. Yacoby, Nat. Commun. **9**, 2712 (2018).
[9] J. Chapman, R. Ploessl, and D. Donnet, Ultramicroscopy **47**, 331 (1992).
[10] D. Song and R. E. Dunin-Borkowski, Phys. Rev. Lett. **127**, 087202 (2021).
[11] T. Zhou, M. Cherukara, and C. Phatak, npj Comput. Mater. **7**, 141 (2021).
[12] Y. Yao, B. Ding, J. Liang, H. Li, X. Shen, R. Yu, and W. Wang, Nat. Commun. **13**, 5991 (2022).
[13] Z. Chen, E. Turgut, Y. Jiang, K. X. Nguyen, M. J. Stolt, S. Jin, D. C. Ralph, G. D. Fuchs, and D. A. Muller, Nat. Nanotechnol. **17**, 1165 (2022).
[14] R. Streubel, J. Mater. Res. **38**, 4977 (2023).
[15] K. L. Mendoza, H. Ni, G. Varnavides, M. Chi, C. Ophus, A. Petford-Long, and C. Phatak, J. Phys. Condens. Matter **37**, 205301 (2025).
[16] A. Kovács, M. Pósfai, B. Zingsem, Z.-A. Li, P. Pekker, J. Caron, S. Prévéral, C. T. Lefèvre, D. A. Bazylinski, R. B. Frankel *et al.*, Geo-Bio Interfaces **1**, e1 (2024).
[17] T. Tanigaki, T. Akashi, T. Yoshida, K. Harada, K. Ishizuka, M. Ichimura, K. Mitsuishi, Y. Tomioka, X. Yu, D. Shindo *et al.*, Nature **631**, 521 (2024).
[18] F. Zheng, V. Migunov, J. Caron, H. Du, G. Pozzi, and R. E. Dunin-Borkowski, Nano Lett. **23**, 843 (2023).
[19] T. Tanigaki, T. Akashi, A. Sugawara, K. Miura, J. Hayakawa, K. Niitsu, T. Sato, X. Yu, Y. Tomioka, K. Harada *et al.*, Sci. Rep. **7**, 16598 (2017).
[20] M. De Graef, N. Nuhfer, and M. McCartney, J. Microsc. **194**, 84 (1999).
[21] M. Beleggia, T. Kasama, and R. E. Dunin-Borkowski, Ultramicroscopy **110**, 425 (2010).
[22] J. Caron, "Model-based reconstruction of magnetisation distributions in nanostructures from electron optical phase images," Ph.D. thesis (RWTH Aachen University, 2017).
[23] H. Lichte and M. Lehmann, Rep. Prog. Phys. **71**, 016102 (2008).
[24] G. Matteucci, G. Missiroli, and G. Pozzi, Adv. Imaging Electron Phys. **122**, 173 (2002).
[25] R. E. Dunin-Borkowski, M. R. McCartney, D. J. Smith, and S. Parkin, Ultramicroscopy **74**, 61 (1998).
[26] K. Keimpema, H. De Raedt, and J. T. M. De Hosson, J. Comput. Theor. Nanosci. **3**, 362 (2006).
[27] T. Prozorov, T. P. Almeida, A. Kovács, and R. E. Dunin-Borkowski, J. R. Soc. Interface **14**, 20170464 (2017).
[28] J. M. Thomas, E. T. Simpson, T. Kasama, and R. E. Dunin-Borkowski, Acc. Chem. Res. **41**, 665 (2008).
[29] J. D. Jackson, *Classical Electrodynamics* (John Wiley & Sons, 1998).
[30] A. Vansteenkiste, J. Leliaert, M. Dvornik, M. Helsen, F. Garcia-Sanchez, and B. Van Waeyenberge, AIP Adv. **4**, 107133 (2014).
[31] W. Williams, A. R. Muxworthy, and G. A. Paterson, J. Geophys. Res. Solid Earth **111**, B12S13, https://doi.org/10.1029/2006JB004556 (2006).
[32] A. R. Muxworthy and W. Williams, J. Geophys. Res. Solid Earth **111**, B12S12, https://doi.org/10.1029/2006JB004588 (2006).
[33] E. Snoeck, C. Gatel, L.-M. Lacroix, T. Blon, S. Lachaize, J. Carrey, M. Respaud, and B. Chaudret, Nano Lett. **8**, 4293 (2008).
[34] C. Gatel, F. J. Bonilla, A. Meffre, E. Snoeck, B. Warot-Fonrose, B. Chaudret, L.-M. Lacroix, and T. Blon, Nano Lett. **15**, 6952 (2015).
[35] Q. Ru, G. Lai, K. Aoyama, J. Endo, and A. Tonomura, Ultramicroscopy **55**, 209 (1994).
[36] J. Su, H. Su, X. Ye, and Z. Li, Opt. Lasers Eng. **184**, 108548 (2025).